

# Bayesian polarization calibration and imaging in very long baseline interferometry

Jong-Seo Kim<sup>1,★</sup>, Jakob Roth<sup>2,3</sup>, Jongho Park<sup>4</sup>, Jack D. Livingston<sup>1</sup>, Philipp Arras<sup>2</sup>, Torsten A. Enßlin<sup>2,5</sup>, Michael Janssen<sup>1,6</sup>, J. Anton Zensus<sup>1</sup>, and Andrei P. Lobanov<sup>1,7</sup>

<sup>1</sup> Max-Planck-Institut für Radioastronomie, Auf dem Hügel 69, D-53121 Bonn, Germany

<sup>2</sup> Max-Planck-Institut für Astrophysik, Karl-Schwarzschild-Str. 1, 85748 Garching, Germany

<sup>3</sup> Technische Universität München (TUM), Boltzmannstr. 3, 85748 Garching, Germany

<sup>4</sup> School of Space Research, Kyung Hee University, 1732, Deogyeong-daero, Giheung-gu, Yongin-si, Gyeonggi-do 17104, Republic of Korea

<sup>5</sup> Ludwig-Maximilians-Universität, Geschwister-Scholl-Platz 1, 80539 Munich, Germany

<sup>6</sup> Department of Astrophysics, Institute for Mathematics, Astrophysics and Particle Physics (IMAPP), Radboud University, P.O. Box 9010, 6500 GL Nijmegen, The Netherlands

<sup>7</sup> Institut für Experimentalphysik, Universität Hamburg, Luruper Chaussee 149, 22761, Hamburg, Germany

Received 20 November 2025 / accepted —

## ABSTRACT

**Context.** Extracting polarimetric information from very long baseline interferometry (VLBI) data is demanding but vital for understanding the synchrotron radiation process and the magnetic fields of celestial objects, such as active galactic nuclei (AGNs). However, conventional CLEAN-based calibration and imaging methods provide suboptimal resolution without uncertainty estimation of calibration solutions, while requiring manual steering from an experienced user.

**Aims.** We present a Bayesian polarization calibration and imaging method for VLBI data sets, that explores the posterior distribution of antenna-based gains, polarization leakages, and polarimetric images jointly from pre-calibrated data.

**Methods.** We reconstructed the posterior distribution of Stokes images, gains, and leakages from real and synthetic data sets in the framework of Bayesian imaging software `resolve` using variational inference methods. Polarization constraints are enforced in the model. Furthermore, polarization calibration with several sources and multiple intermediate frequencies (IFs) is supported in order to maximize the parallactic angle coverage and identify instrumental corruptions per IF.

**Results.** We demonstrate our calibration and imaging method with observations of the quasar 3C273 with the Very Long Baseline Array (VLBA) at 15 GHz and the blazar OJ287 with the Global Millimeter VLBI Array (GMVA) + Atacama Large Millimeter/Submillimeter Array (ALMA) at 86 GHz. Compared to the CLEAN method, our approach provides physically realistic images that satisfy positivity of flux and polarization constraints and can reconstruct complex source structures composed of various spatial scales. In contrast to conventional imaging and calibration methods, our method systematically accounts for calibration uncertainties in the final images and provides uncertainties of Stokes images and calibration solutions.

**Conclusions.** Our Bayesian polarization calibration and imaging method explores the posterior distribution of calibration solutions and reconstruct physically plausible high-resolution images from VLBI data. The automated Bayesian approach for calibration and imaging will be able to obtain high-fidelity polarimetric images using high-quality data from next-generation radio arrays. The pipeline developed for this work is publicly available.

**Key words.** techniques: interferometric - techniques: image processing - techniques: high angular resolution - methods: statistical - polarization - galaxies: active - galaxies: jets

## 1. Introduction

Polarization provides valuable information about astronomical objects and the ambient medium in astronomy, as it is one of the most direct ways to access information about astrophysical magnetic fields. In conjunction with very long baseline interferometry (VLBI), which is able to achieve nominal resolutions of  $\sim 20 \mu\text{as}$  at 1 mm (Event Horizon Telescope Collaboration et al. 2019) and  $\sim 15 \mu\text{as}$  at 345 GHz (Raymond et al. 2024), we have the ability to probe extreme magneto-ionic environments.

Polarimetric studies with VLBI have revealed the presence of helical and toroidal magnetic fields in the jet of AGN (Asada et al. 2008; Hovatta et al. 2012; Gabuzda et al. 2017), the magnetic field of the supermassive black holes M87\* and Sgr A\*

(Event Horizon Telescope Collaboration et al. 2021, 2024; Event Horizon Telescope Collaboration 2025), and an alignment between polarization and the jets of AGN, suggesting the presence of magnetizing shocks in AGN jets (Lister & Homan 2005; Pushkarev et al. 2023). However, polarization calibration of VLBI data is challenging, as polarization signals typically have signal-to-noise ratios (S/N) that are an order of magnitude lower than for total intensity.

Polarized data after pre-calibration can still have significant residual corruption from leakage between one polarization feed to another, known as polarization leakage or ‘D-terms’. Moreover, the complex source structure of calibrators in VLBI, especially at mm-wavelengths, hinders the estimation of this polarization leakage. The conventional polarization calibration approach in radio interferometry is observing a static and point-

\* jongkim@mpifr-bonn.mpg.de

like calibrator with known polarization properties and identifying leakage corruptions by using the information about the calibrator and disentangling source polarization from the instrumentation contributions that are being solved by the time-varying polarization of the feed angle rotation. However, due to the high angular resolution, it is unusual to find static point-like calibrators for polarization calibration in VLBI (Cotton 1993).

Leppanen et al. (1995) introduced the **LPCAL** software to infer polarization leakage corruptions in VLBI data sets. **LPCAL** utilizes a polarization prior model with a set of components which assumes that the linear polarization of a component is proportional to the total intensity of the corresponding component, known as the similarity approximation (Cotton 1993; Leppanen et al. 1995). The simple and effective prior is advantageous in order to determine leakage corruption from sparse and noisy VLBI data sets due to the small number of degrees of freedom in the model.

However, the similarity approximation in **LPCAL** is not valid for sources with complex polarization structure (Cotton 1993). Furthermore, multi-source calibration is not directly supported (see Lister & Homan 2005, for an example of a multi-source method with **LPCAL**) and D-terms are considered both static in time and frequency for each intermediate frequency (IF) as default in **LPCAL**. Recently, the new **CLEAN**-based polarization calibration software packages **GPCAL** (Park et al. 2021b) and **PolSolve** (Martí-Vidal et al. 2021) are able to employ reconstructed Stokes Q and U images as priors in leakage calibration, a technique called polarization self-calibration. These software support multi-source models to increase parallactic angle coverage, and are able to solve for D-terms that vary with time and frequency.

Nevertheless, **GPCAL** and **PolSolve** still rely on the conventional **CLEAN** deconvolution algorithm, which has limitations. The **CLEAN** algorithm is supervised and user-dependent. As a result, **CLEAN** windows and weighting schemes may induce biases in the final results. Furthermore, **CLEAN** assumes that the sky is a collection of point sources (usually of the size of the synthesized beam) or Gaussian blobs in multi-scale **CLEAN** (Cornwell 2008), but has no explicit notion of an extended structure. This results in suboptimal resolution, as the potential of radio interferometric observations to super-resolve sources (in the high S/N regime) is not exploited. Consequently, the **CLEAN** image model for the leakage calibration is not suitable for radio interferometric data with complex source structure. Moreover, the conventional **CLEAN**-based self-calibration is performed iteratively with switching between flagging and manually choosing gain solution intervals that results in inconsistent calibration solutions (Martí-Vidal & Marcaide 2008; Popkov et al. 2021) and a lack of reproducibility. Lastly, calibration uncertainties are not taken into account in the final results and uncertainty estimation is not supported.

Modern forward modeling imaging algorithms provide us a new approach to overcome the limitations of **CLEAN**-based polarization calibration methods (Birdi et al. 2020; Pesce 2021; Event Horizon Telescope Collaboration et al. 2021, 2024). Explicit regularizers and prior assumptions in forward modeling algorithms enable us to infer more robust leakage solutions from sparse VLBI data sets. For example, polarization constraints can be enforced in the polarization imaging model to avoid unphysical polarimetric images (Birdi et al. 2018). Recent instrumental advancement in VLBI accomplishes significantly improved S/N and more wide-band observations. Additionally, the latest algorithmic developments offer methods to solve highly degenerate inverse problems efficiently. A modern polarization calibration

and imaging pipeline that utilizes the full potential of the data is highly desirable.

In this work, we introduce a novel Bayesian calibration and imaging method using the Bayesian imaging software **resolve**. The posterior distribution of antenna-based gains, D-terms, and Stokes images are explored jointly using variational inference algorithms (Knollmüller & Enßlin 2019; Frank et al. 2021). Recently, the polarization constraint ( $I \geq \sqrt{Q^2 + U^2 + V^2}$ ) is encoded in the the **resolve** polarization imaging model (Arras et al. 2025). We utilize this polarization imaging model and incorporate polarization calibration and gain self-calibration directly into the imaging process. Furthermore, multi-source and multi-IF polarization calibration are supported in a probabilistic framework.

This article is structured as follows. In section 2, we explain the conventional **CLEAN**-based polarization calibration method and our Bayesian method. In section 3 and section 4, we validate the method with synthetic and real data sets respectively. We summarize our results in section 5.

## 2. Method

### 2.1. Radio Interferometer measurement equation (RIME)

A radio interferometer measures Fourier components of the sky brightness distribution instead of imaging the sky directly. According to the van Cittert-Zernike theorem, the two-point correlation function of the signals recorded by two antennas,  $i$  and  $j$ , called the visibility data  $V_{ij}$ , is given by the Fourier transformed sky brightness distribution  $I$  for total intensity under the assumption that the field of view is small (Hamaker et al. 1996; Smirnov 2011; Thompson et al. 2017):

$$V(u, v)_{ij} = \int_{-\infty}^{\infty} \int_{-\infty}^{\infty} I(x, y) e^{-2\pi i(ux+vy)} dx dy = \text{FT}[I], \quad (1)$$

where  $(u, v)$  are the Fourier domain coordinates,  $(x, y)$  are the image domain coordinates, and  $\text{FT}$  is the Fourier transform operator.

Since the observed data is incomplete and corrupted by atmospheric and instrumental effects, we obtain a low-fidelity image, also known as the dirty map, from a direct Fourier transform of the visibility data. Inferring the real source structure from radio interferometric data is an ill-posed inverse problem, and therefore a unique solution does not exist. Thus, additional assumptions, prior knowledge, or other regularizers of the solution space are required to obtain high-fidelity images from radio interferometric data in image reconstruction.

The measurement equation (Eq. 1) can be generalized for full polarization observation, and the instrumental and atmospheric data corruption can be described by Jones matrices (Jones 1941). As a result, the radio interferometer measurement equation (RIME) for the full polarimetric visibility matrix  $\mathbf{V}$  in the circular polarization basis is given by (Smirnov 2011):

$$\mathbf{V}_{ij} = \mathbf{J}_i \left( \int_{-\infty}^{\infty} \int_{-\infty}^{\infty} \mathbf{I}(x, y) e^{-2\pi i(ux+vy)} dx dy \right) \mathbf{J}_j^\dagger + \mathbf{N}_{ij}, \quad (2)$$

where  $\mathbf{V}_{ij}$  is the visibility matrix consisting of four complex correlation functions by the signal from the right-hand circular polarization (RCP)  $R$  and the signal from the left-hand circular polarization (LCP)  $L$ :

$$\mathbf{V}_{ij} = \begin{pmatrix} R_i R_j^* & R_i L_j^* \\ L_i R_j^* & L_i L_j^* \end{pmatrix}, \quad (3)$$

where the asterisk  $*$  denotes a complex conjugate.  $\mathbf{J}_i$  is the Jones matrix describing the data corruption of the antenna  $i$  by instrumental and atmospheric effects:

$$\mathbf{J}_i = \mathbf{G}_i \mathbf{D}_i \mathbf{P}_i = \begin{pmatrix} g_i^R & 0 \\ 0 & g_i^L \end{pmatrix} \begin{pmatrix} 1 & D_i^R \\ D_i^L & 1 \end{pmatrix} \begin{pmatrix} e^{-i\phi_i} & 0 \\ 0 & e^{i\phi_i} \end{pmatrix}, \quad (4)$$

where  $\mathbf{G}_i$  is the antenna-based gain matrix,  $\mathbf{D}_i$  is the leakage (D-term) matrix describing the signal leakage between polarizers (e.g.,  $D_i^R$  is the signal leakage from LCP to RCP for antenna  $i$ ),  $\mathbf{P}_i$  is the field rotation angle matrix,  $\dagger$  denotes conjugate transposition,  $\mathbf{N}_{ij}$  is the additive noise, and  $\mathbf{I}$  is the polarimetric sky brightness distribution matrix, consisting of Stokes  $I$ ,  $Q$ ,  $U$ , and  $V$ :

$$\mathbf{I} = \begin{pmatrix} I + V & Q + iU \\ Q - iU & I - V \end{pmatrix}. \quad (5)$$

The antenna field rotation angle  $\phi$ , representing the rotation of the receiver polarization feeds with respect to the source due to Earth's rotation, is defined as  $\phi = f_{\text{el}}\theta_{\text{el}} + f_{\text{par}}\psi_{\text{par}} + \phi_{\text{off}}$ , where  $\theta_{\text{el}}$  is the elevation angle,  $\psi_{\text{par}}$  is the parallactic angle, and  $\phi_{\text{off}}$  is a constant offset. The field rotation angle depends on the antenna mount. Alt-azimuth (ALT-AZ) mounts with a Cassegrain focus have  $f_{\text{par}} = 1$  and  $f_{\text{el}} = 0$ . ALT-AZ mounts with a Nasmyth-Right type focus have  $f_{\text{par}} = 1$  and  $f_{\text{el}} = 1$ , and ALT-AZ mounts with a Nasmyth-Left type focus have  $f_{\text{par}} = 1$  and  $f_{\text{el}} = -1$ . More details regarding the antenna mount types can be found in the Appendix C of Janssen et al. (2019).

The polarization calibration and imaging model with the polarimetric visibility matrix data  $\mathbf{V}$ , Jones matrices  $\mathbf{J}_i$ ,  $\mathbf{J}_j$  for antennas,  $i$  and  $j$ , and model visibilities ( $\mathcal{RR}$ ,  $\mathcal{RL}$ ,  $\mathcal{LR}$ , and  $\mathcal{LL}$ ) from Stokes images is

$$\begin{aligned} R_i R_j^* &= g_i^R g_j^{R*} [e^{-i\phi_i} \mathcal{RR} e^{i\phi_j} + D_i^R e^{i\phi_i} \mathcal{LR} e^{i\phi_j} \\ &\quad + e^{-i\phi_i} \mathcal{RL} e^{-i\phi_j} D_j^{R*} + D_i^R e^{i\phi_i} \mathcal{L} \mathcal{L} e^{-i\phi_j} D_j^{R*}] \\ R_i L_j^* &= g_i^R g_j^{L*} [e^{-i\phi_i} \mathcal{RR} e^{i\phi_j} D_j^{L*} + D_i^R e^{i\phi_i} \mathcal{LR} e^{i\phi_j} D_j^{L*} \\ &\quad + e^{-i\phi_i} \mathcal{RL} e^{-i\phi_j} + D_i^R e^{i\phi_i} \mathcal{L} \mathcal{L} e^{-i\phi_j}] \\ L_i R_j^* &= g_i^L g_j^{R*} [D_i^L e^{-i\phi_i} \mathcal{RR} e^{i\phi_j} + e^{i\phi_i} \mathcal{LR} e^{i\phi_j} \\ &\quad + D_i^L e^{-i\phi_i} \mathcal{RL} e^{-i\phi_j} D_j^{R*} + e^{i\phi_i} \mathcal{L} \mathcal{L} e^{-i\phi_j} D_j^{R*}] \\ L_i L_j^* &= g_i^L g_j^{L*} [D_i^L e^{-i\phi_i} \mathcal{RR} e^{i\phi_j} D_j^{L*} + e^{i\phi_i} \mathcal{LR} e^{i\phi_j} D_j^{L*} \\ &\quad + D_i^L e^{-i\phi_i} \mathcal{RL} e^{-i\phi_j} + e^{i\phi_i} \mathcal{L} \mathcal{L} e^{-i\phi_j}], \end{aligned} \quad (6)$$

where the model visibility matrix consists of Stokes images:

$$\mathbf{V}_{\text{model}} = \begin{pmatrix} \mathcal{RR} & \mathcal{RL} \\ \mathcal{LR} & \mathcal{LL} \end{pmatrix} = \mathbb{FT} \left[ \begin{pmatrix} I + V & Q + iU \\ Q - iU & I - V \end{pmatrix} \right]. \quad (7)$$

Polarization calibration and imaging is equivalent to estimating the gains  $g$ , D-terms  $D$ , Stokes images  $I$ ,  $Q$ ,  $U$ , and  $V$  from the visibility data  $\mathbf{V}$ . In the conventional CLEAN-based method, this polarimetric calibration and imaging problem in VLBI is solved in an iterative fashion since the problem is highly degenerate. In this work, we infer the gains  $g$ , leakages  $D$ , Stokes  $I$ ,  $Q$ ,  $U$ , and  $V$  jointly from pre-calibrated visibility matrix data  $\mathbf{V}$  in a probabilistic approach.

## 2.2. CLEAN-based polarization calibration method

The CLEAN-based polarization calibration method assumes that the antenna gains have already been calibrated during the data pre-processing and imaging/self-calibration procedures. It also assumes that the antenna's field rotation angles have been corrected during the data pre-processing phase (see Park et al. 2021b, 2023; Martí-Vidal et al. 2021 for more details). With these assumptions, the cross-hand visibilities consist of both the source's intrinsic linear polarization terms and the terms associated with the antenna's polarimetric leakages and field rotation angles.

Determining the leakages is not straightforward, as they need to be disentangled from the source polarization terms. One of the most widely used methods in the past assumes that the source's linear polarization emission is proportional to the total intensity structure within each "sub-model", which consists of a group of neighboring total intensity CLEAN components. This method is known as the "similarity approximation" (Cotton 1993; Leppänen et al. 1995) and is implemented in LPCAL, a task within the Astronomical Image Processing System (AIPS; Greisen (2003)).

While generally a good approximation, the similarity method faces challenges when dealing with very weakly polarized sources (e.g., Park et al. 2021a), particularly when utilizing global VLBI observations at millimeter wavelengths, which provide ultra-high angular resolution. In such cases, the source's linear polarization structures are often complex, and the similarity approximation may not hold well (e.g., Event Horizon Telescope Collaboration et al. 2021, 2024; Zhao et al. 2022).

To overcome this limitation, two methods have been developed: GPCAL (Park et al. 2021b), based on AIPS and Difmap, and PolSolve (Martí-Vidal et al. 2021), based on CASA (CASA Team et al. 2022). These methods conduct calibration as follows:

1. They derive the leakages using the similarity approximation, like LPCAL, and remove them from the data.
2. They perform imaging with CLEAN using the leakage-corrected data to obtain the source's Stokes  $Q$  and  $U$  CLEAN models.
3. They use the original data to derive the leakage solutions again, this time using the source's linear polarization models obtained in the previous step, and remove the leakages using the updated solutions.
4. They iteratively update the source's linear polarization models and leakage solutions by repeating steps 2 and 3 until the solutions converge.

These methods can also simultaneously utilize data from multiple calibrator sources, which typically leads to improved leakage calibration accuracy, as the leakage solutions are not expected to vary between sources.

## 2.3. Bayesian imaging software resolve

The open-source Bayesian imaging software `resolve`<sup>1</sup> treats radio interferometric imaging and calibration (Eq. 2) as an inverse problem and computes a probabilistic solution for it. Thus, `resolve` computes the probability distribution of the sky brightness  $\mathbf{I}$  given the measured visibilities. In Arras et al. (2019b), a joint calibration and imaging approach was introduced, computing a posterior probability distribution for the sky brightness  $\mathbf{I}$  and the antenna gains  $\mathbf{G}$ . Roth et al. (2023) extended this approach, incorporating direction-dependent effects in the antenna

<sup>1</sup> <https://gitlab.mpcdf.mpg.de/ift/resolve>

gains. A further extension to `resolve` was made in Arras et al. (2025), enabling full Stokes imaging. In Roth et al. (2024), the idea of major and minor cycles used in CELAN based algorithms was adapted in a Bayesian version for the `resolve` framework.

Building on the full Stokes imaging capabilities, this work introduces polarization calibration and imaging to `resolve`. Thus, we compute the posterior distribution of the full Stokes sky brightness matrix  $\mathbf{I}$  jointly with the posterior distributions of the antenna-based gain matrix  $\mathbf{G}$ , and leakage matrix  $\mathbf{D}$ . The posterior distribution can be expressed via Bayes' theorem

$$\mathcal{P}(\mathbf{G}, \mathbf{D}, \mathbf{I} | \mathbf{V}) = \frac{\mathcal{P}(\mathbf{V} | \mathbf{G}, \mathbf{D}, \mathbf{I}) \mathcal{P}(\mathbf{G}, \mathbf{D}, \mathbf{I})}{\mathcal{P}(\mathbf{V})}, \quad (8)$$

in terms of the likelihood  $\mathcal{P}(\mathbf{V} | \mathbf{G}, \mathbf{D}, \mathbf{I})$  and the prior  $\mathcal{P}(\mathbf{G}, \mathbf{D}, \mathbf{I})$ . In the following section 2.4, we discuss the likelihood model. In section 2.5, we outline the prior models and in section 2.6, we describe the algorithm for approximating the posterior distribution given the likelihood and prior.

#### 2.4. Likelihood distribution

As outlined in Section 2.3, we approach the polarization calibration and imaging problem as a Bayesian inference task. This entails defining the prior and likelihood to compute the posterior distribution, which represents the result of the Bayesian imaging/inference process.

Following the framework established by Knollmüller & Enßlin (2018), we employ a coordinate transformation, or reparametrization trick (also known as inverse transform sampling), to introduce new parameters  $\xi$ . This transformation ensures that the prior follows a standard normal distribution  $\mathcal{P}(\xi) = \mathcal{G}(\xi, 1)$ , integrating all prior knowledge into the likelihood component  $\mathcal{P}(\mathbf{V} | \xi)$ .

The likelihood  $\mathcal{P}(\mathbf{V} | \xi)$  is composed of two components:  $\mathcal{P}(\mathbf{V} | \mathbf{G}, \mathbf{D}, \mathbf{I})$  and a function of mapping  $\xi$  to specific values of  $\mathcal{G}$ ,  $\mathcal{D}$ , and  $\mathcal{I}$ . The former component describes the data aspect of the likelihood while the latter incorporates the prior information for the gains  $g$ , the leakages  $D$ , and the Stokes images  $I, Q, U$ , and  $V$ . This section elaborates on the first component while the following section will deal with the second.

Our data model integrates gain matrices  $\mathbf{G}$ , leakage matrices  $\mathbf{D}$ , field rotation angle matrices  $\mathbf{P}$ , and the polarization imaging model  $\mathbf{I}$ . Upon setting  $\mathbf{G}$ ,  $\mathbf{D}$ ,  $\mathbf{P}$ , and  $\mathbf{I}$ , the visibility data  $\mathbf{V}$  can be formulated as follows:

$$\mathbf{V}_{ij} = \mathbf{G}_i \mathbf{D}_i \mathbf{P}_i \text{FT}[\mathbf{I}] \mathbf{P}_j^\dagger \mathbf{D}_j^\dagger \mathbf{G}_j^\dagger. \quad (9)$$

By encapsulating Jones matrices into the response function, the model can be simplified:

$$\mathbf{V}_{ij} = \mathbf{J}_i \text{FT}[\mathbf{I}] \mathbf{J}_j^\dagger = \mathbf{R}^{(g, D)}[\mathbf{I}], \quad (10)$$

where  $\mathbf{R}^{(g, D)}$  is the response function consisting of the Fourier operator and Jones matrices.

It is important to note that field rotation angle matrices  $\mathbf{P}$  are often pre-corrected during pre-calibration to stabilize the phase calibration in VLBI. However, the field rotation angle matrix  $\mathbf{P}$  and the D-term matrix  $\mathbf{D}$  are not commutative. Consequently, our model for pre-corrected field rotation angle data is:

$$\mathbf{V}_{ij}^{\phi \text{ cor.}} = \mathbf{P}_i^{-1} \mathbf{G}_i \mathbf{D}_i \mathbf{P}_i \text{FT}[\mathbf{I}] \mathbf{P}_j^\dagger \mathbf{D}_j^\dagger \mathbf{G}_j^\dagger (\mathbf{P}_j^\dagger)^{-1}. \quad (11)$$

This means we must reverse the pre-correction of the field rotation angle in pre-calibrated data before adequately solving the

Jones matrices, given the non-commutative properties of matrices  $\mathbf{G}$ ,  $\mathbf{D}$ , and  $\mathbf{P}$ .

Assuming additive Gaussian noise on the radio interferometric data, justified by the central limit theorem, the likelihood given noise covariance  $\mathbb{N}$  is expressed as:

$$\mathcal{P}(\mathbf{V} | \mathbf{I}, \mathbf{G}, \mathbf{D}) = \mathcal{G}(\mathbf{V} - \mathbf{R}^{(g, D)}[\mathbf{I}], \mathbb{N}). \quad (12)$$

In this work, the noise covariance is assumed to have a diagonal covariance; thus, the noise is uncorrelated. This likelihood formulation underscores how our method, unlike CLEAN-based polarization calibration methods, facilitates the simultaneous inference of calibration solutions and Stokes images. Consequently, the uncertainty estimation of Stokes images inherently reflects uncertainties from the calibration, data noise and incomplete uv-coverage.

**Table 1.** List of prior distributions in the Bayesian polarization calibration and imaging model.

Model	Description	Prior
$s$	Polarization imaging model	2D $\mathcal{GP}(\xi_s)$
$q$	Polarization imaging model	2D $\mathcal{GP}(\xi_q)$
$u$	Polarization imaging model	2D $\mathcal{GP}(\xi_u)$
$v$	Polarization imaging model	2D $\mathcal{GP}(\xi_v)$
$\lambda$	Log-normal amplitude gain	1D $\mathcal{GP}(\xi_\lambda)$
$\phi$	Phase gain	1D $\mathcal{GP}(\xi_\phi)$ or $\mathcal{N}(0, \sigma_\phi^2)$
$a$	Log-normal amplitude D-term	$\mathcal{N}(m_a, \sigma_a^2)$
$b$	Phase D-term	$\mathcal{N}(0, \sigma_b^2)$

#### 2.5. Polarization calibration and imaging prior model

As detailed in Section 2.4, we transform the imaging problem such that the formal prior distribution is a standard normal distribution:  $\mathcal{G}(\xi, 1)$ . Using this reparametrization method, specifying the prior translates to defining generative models, which use standard-normal distributed parameters as inputs to generate the variables of interest, such as the full Stokes sky model  $\mathbf{I}$ , the gain matrices  $\mathbf{G}$ , and the leakage matrices  $\mathbf{D}$ .

**Generative model for polarization imaging prior  $\mathbf{I}$**  The generative model for the Stokes sky emission  $\mathbf{I}$  closely follows the model presented in Arras et al. (2025). Regarded as a complex  $2 \times 2$  matrix,  $\mathbf{I}$  is defined by:

$$\mathbf{I} = \begin{pmatrix} \langle E_{i,r} E_{j,r}^* \rangle & \langle E_{i,r} E_{j,l}^* \rangle \\ \langle E_{i,l} E_{j,r}^* \rangle & \langle E_{i,l} E_{j,l}^* \rangle \end{pmatrix} = \begin{pmatrix} I + V & Q + iU \\ Q - iU & I - V \end{pmatrix}, \quad (13)$$

within the circular basis (Smirnov 2011). Here,  $E$  is the electric field, and indices  $i, j$  denote antenna labels and  $r, l$  refer to the respective circular feeds. The matrix must meet specific constraints: (1)  $\mathbf{I}$  is positive definite and Hermitian, (2) strictly positive total flux  $I > 0$ , and (3) an upper bound on polarized emission  $I^2 \geq Q^2 + U^2 + V^2$  (Hamaker et al. 1996; Smirnov 2011).

Arras et al. (2025) identifies the matrix exponential as a fitting parametrization for the polarized sky brightness distribution:

$$\mathbf{I} = e^x := \exp \begin{pmatrix} s + v & q + \mathbf{i}u \\ q - \mathbf{i}u & s - v \end{pmatrix}, \quad (14)$$

where  $s, q, u$ , and  $v$  are real numbers for each pixel, in particular they can be both positive and negative.

Stokes  $I, Q, U$ , and  $V$  can be obtained from the two dimensional fields  $s, q, u$ , and  $v$ :

$$\begin{aligned} I &= e^s \cosh p, & Q &= \frac{q}{p} e^s \sinh p, \\ U &= \frac{u}{p} e^s \sinh p, & V &= \frac{v}{p} e^s \sinh p, \end{aligned} \quad (15)$$

where  $p := \sqrt{q^2 + u^2 + v^2}$ .

The total flux  $I$  is strictly positive in Equation 15 and  $\mathbf{I}$  is Hermitian since the matrix exponential and the Hermitian conjugate commute. Furthermore,  $\mathbf{I}$  is positive definite because the eigenvalues of a Hermitian matrix are real and the eigenvalues of the matrix exponential are the exponential of the eigenvalues. The determinant of  $\mathbf{I}$  is the product of the eigenvalues, which is positive:

$$0 < \det \mathbf{I} = I^2 - Q^2 - U^2 - V^2. \quad (16)$$

Thus, it proves that this parametrization satisfies all three conditions of  $\mathbf{I}$ .

To complete the generative model for  $\mathbf{I}$ , we need to define the models generating the 2-dimensional (2D) fields  $s, q, u$ , and  $v$ . We model each of those fields using a Gaussian process ( $\mathcal{GP}$ ) with a non-parametric correlation kernel, captured through generative models that convert standard-normal distributed latent parameters  $\xi_s, \xi_q, \xi_u, \xi_v$  into the Gaussian process values  $s(\xi_s), q(\xi_q), u(\xi_u), v(\xi_v)$  (following methods in Arras et al. (2021)). In our polarization imaging prior model, the spatial correlation between pixels and the correlation between Stokes images are taken into account since the correlation kernels of  $s, q, u$ , and  $v$  are inferred from the data. The exact mathematical definition of the generative Gaussian process model can be found in Arras et al. (2021, Sec. 3.4).

**Generative model for gain prior  $g$**  The antenna based gain prior consists of two Gaussian process models is

$$g(t) = \exp(\lambda(t) + \mathbf{i}\phi(t)), \quad (17)$$

where log-normal amplitude gain  $\lambda$  and phase gain  $\phi$  are 1-dimensional (1D) Gaussian process priors.

For the gain prior, we use the same generative Gaussian process model in the imaging prior. Thus, the log-normal amplitude gain  $\lambda(\xi_\lambda)$  and phase gain  $\phi(\xi_\phi)$  can be described by standard-normal distributed model parameters  $\xi_\lambda$  and  $\xi_\phi$ . For mm-VLBI data with short phase coherence time, we can use an uncorrelated normal-distribution  $\phi \sim \mathcal{N}(0, \sigma_\phi^2)$  for the phase gain prior.

In **resolve**, the temporal correlation structures in gain solutions are inferred from the data. In order words, we determine the gain solution interval from the data without manual steering and we are even able to infer solution interval per antennas, which can be advantageous for data from a heterogeneous VLBI array (Kim et al. 2025). More details about the antenna-based gain calibration in **resolve** can be found in (Arras et al. 2019b; Kim et al. 2024).

**Generative model for D-term prior  $D$**  The D-term (leakage) prior model is given by:

$$D = \exp(a + \mathbf{i}b), \quad (18)$$

where  $a \sim \mathcal{N}(m_a, \sigma_a^2)$  and  $b \sim \mathcal{N}(0, \sigma_b^2)$  are normal distributed priors,  $m_a$  is the mean of the log-normal amplitude D-term, and  $\sigma_a$  and  $\sigma_b$  are the standard deviations of the log-normal amplitude and phase D-term respectively.

Therefore, the D-term amplitude is log-normal distributed and the D-term phase is normal distributed. A summary table in Table 1 describes our calibration and imaging prior models.

## 2.6. Posterior distribution

The posterior distribution of all unknowns given the visibility data in Equation 8 is a very high dimensional object including the Stokes images, gains, and D-terms. Due to the high number of dimensions and the complicated relations between all the involved quantities, any representation of this probability function needs an approximation. One way of representing a posterior distribution is via a set of samples drawn from it. Be  $\mathbf{s} = (\mathbf{I}, \mathbf{G}, \mathbf{D})$  denotes the quantities to be inferred and  $\mathbf{d} = \mathbf{V}$  denotes the data, then the samples  $\mathbf{s}_i \leftrightarrow \mathcal{P}(\mathbf{s}|\mathbf{d})$  with  $i \in \{1, \dots, N\}$  are an approximative representation of the posterior  $\mathcal{P}(\mathbf{s}|\mathbf{d})$  as any expectation with respect to some function  $f(\mathbf{s})$  can be calculated from those approximately,

$$\langle f(\mathbf{s}) \rangle_{(\mathbf{s}|\mathbf{d})} := \int \mathcal{D}\mathbf{s} f(\mathbf{s}) \mathcal{P}(\mathbf{s}|\mathbf{d}) \approx \frac{1}{N} \sum_{i=1}^N f(\mathbf{s}_i), \quad (19)$$

where  $\int \mathcal{D}\mathbf{s}$  indicates a path integral.

In this work, we utilized two variational inference algorithms (MGVI, geoVI) (Knollmüller & Enßlin 2019; Frank et al. 2021) as implemented in the NIFTy software package (Selig et al. 2013; Arras et al. 2019a) to explore the posterior distribution of the Stokes images and calibration solutions. In the variational inference method, the posterior distribution is approximated as a parametrized distribution by minimizing the Kullback-Leibler (KL) divergence as a cost function. The KL divergence measures the information gain between two probability distributions.

These variational inference methods scale quasi-linearly in computational complexity with the problem size; therefore, they enable to solve high-dimensional calibration and imaging problems. Specifically, geoVI, an extension of the MGVI algorithm, can describe non-Gaussian posteriors by constructing a coordinate transformation between the latent space, in which the prior was Gaussian, but the posterior is not, to another latent space, in which the posterior becomes approximate Gaussian. More details about MGVI and geoVI can be found in (Knollmüller & Enßlin 2019; Frank et al. 2021).

From the posterior samples, the posterior mean of the fractional linear polarization is

$$\langle P_{\text{frac}}(\mathbf{s}) \rangle_{(\mathbf{s}|\mathbf{d})} := \int \mathcal{D}\mathbf{s} \left( \frac{Q(\mathbf{s})^2 + U(\mathbf{s})^2}{I(\mathbf{s})^2} \right) \mathcal{P}(\mathbf{s}|\mathbf{d}) = \left\langle \frac{Q^2 + U^2}{I^2} \right\rangle. \quad (20)$$

We note that the posterior mean of the fractional linear polarization is not equal to  $\langle Q^2 + U^2 \rangle / \langle I^2 \rangle$ , where  $\langle I \rangle, \langle Q \rangle$ , and  $\langle U \rangle$

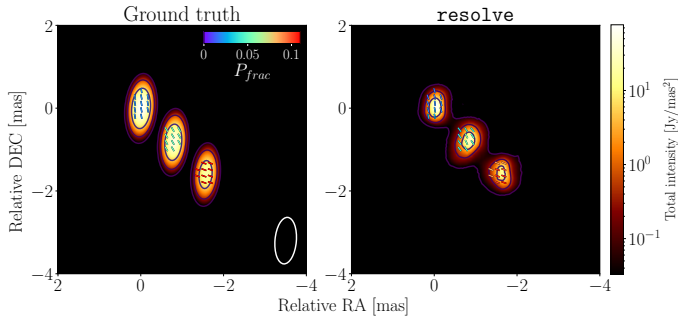


**Fig. 1.** Comparison between the ground truth image (left panel) convolved with the nominal CLEAN beam with the uniform weighting and the posterior mean resolve polarization reconstruction (right panel) with EVPAs with colors corresponding to the fractional linear polarization  $P_{\text{frac}}$ . The contours represent the total intensity of corresponding images.

are the posterior mean Stokes images, because of the non-linear dependence of  $P_{\text{frac}}$  on the Stokes parameters.

As another example, the posterior mean of the electric vector position angle (EVPA) is

$$\langle \Phi \rangle_{(\mathbf{s}|\mathbf{d})} := \int \mathcal{D}\mathbf{s} \frac{1}{2} \arctan\left(\frac{U(\mathbf{s})}{Q(\mathbf{s})}\right) \mathcal{P}(\mathbf{s}|\mathbf{d}) = \left\langle \frac{1}{2} \arctan\left(\frac{U}{Q}\right) \right\rangle. \quad (21)$$

### 3. Application to synthetic data

In VLBI, polarization calibration using multiple calibrators at different declinations helps to reconstruct more robust leakage solutions, which break the degeneracy between the field rotation angle matrix  $\mathbf{P}$  and the leakage matrix  $\mathbf{D}$  (Park et al. 2021b; Martí-Vidal et al. 2021). In order to validate the Bayesian polarization calibration method with multiple calibrators, we tested our method with three of the synthetic VLBA data sets presented in Park et al. (2021b). Synthetic data sets were produced using PolSimulate in the CASA software (McMullin et al. 2007) with OJ287, 3C273, BLLac uv-coverage at 15GHz by 10 VLBA antennas. More details regarding the synthetic data can be found in Park et al. (2021b). The ground truth image consists of three point sources. The ground truth image convolved with the nominal CLEAN beam with the uniform weighting is in Figure 1. We assume that there is no gain corruption in the data.

The polarization calibration with synthetic data was performed as follows. First of all, initial D-term estimates were obtained by the maximum a-posteriori (MAP) method using all three calibrator data sets. Then, the posterior distribution of Stokes images and D-term was reconstructed with 3C273 synthetic data using the geoVI method (Frank et al. 2021) starting from estimated MAP D-terms as the initial condition. Figure 1 shows the resolve total intensity image and EVPAs with colors corresponding to the fractional linear polarization (right panel). We chose a spatial domain of  $256 \times 256$  pixels and a field of view of  $10 \text{ mas} \times 10 \text{ mas}$ . The resolve image was able to recover three linearly polarized components (with the fractional linear polarization 2%, 5%, and 11% respectively).

Figure 2 represents a comparison between the resolve D-term posterior distribution and the ground truth D-terms. The resolve posterior distribution is obtained from 100 posterior samples using Gaussian kernel density distribution in Scipy Python library (Virtanen et al. 2020). Overall, the reconstructed D-term posterior distributions using resolve are consistent with

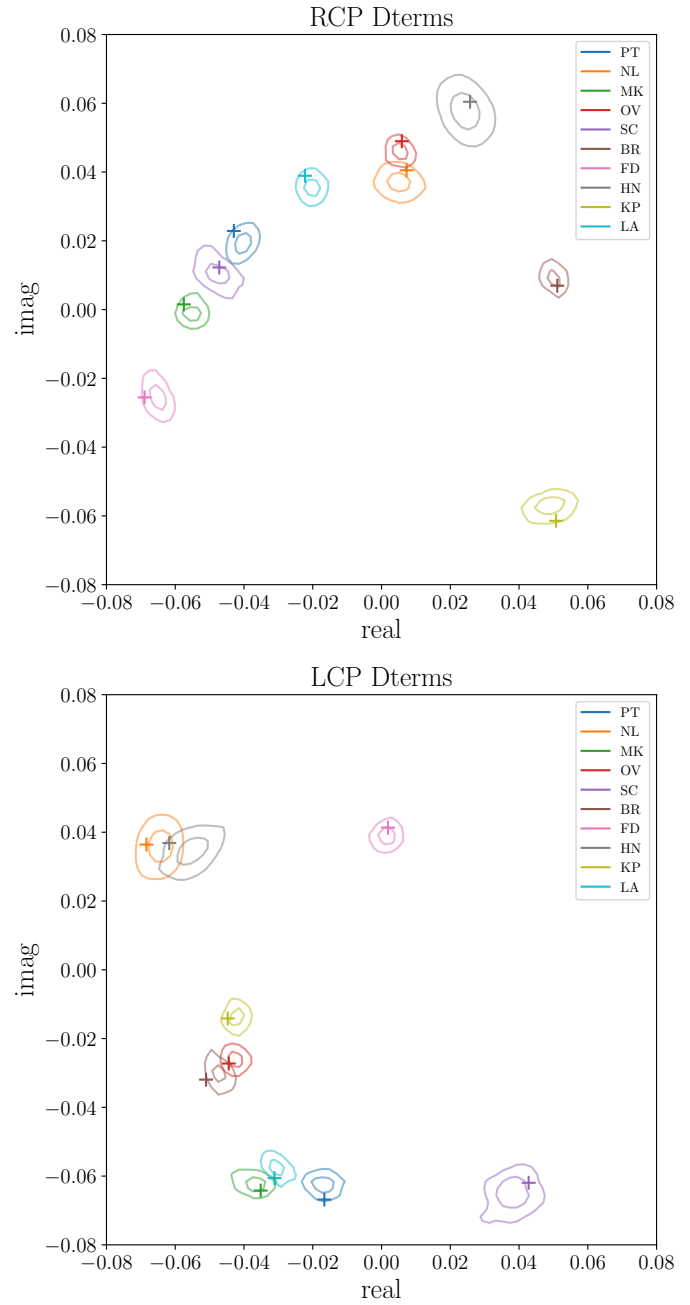


**Fig. 2.** Comparison between the D-term posterior using **resolve** and ground truth D-terms from the synthetic data. Contours show  $1\sigma$  and  $2\sigma$  cumulative regions of resolve posterior D-terms using Gaussian kernel density estimation. The plus signs correspond to the ground truth D-terms.

the ground truth D-terms within the  $2\sigma$  errors. This results demonstrate that the resolve polarization calibration and imaging method is able to reconstruct reliable D-term solutions and Stokes images using multiple calibrator data sets.

### 4. Application to real data

#### 4.1. 3C273 VLBA observation at 15 GHz

We applied our Bayesian polarization calibration and imaging method to pre-calibrated (without self-calibration and D-term calibration) 3C273 VLBA MOJAVE survey data at 15 GHz on

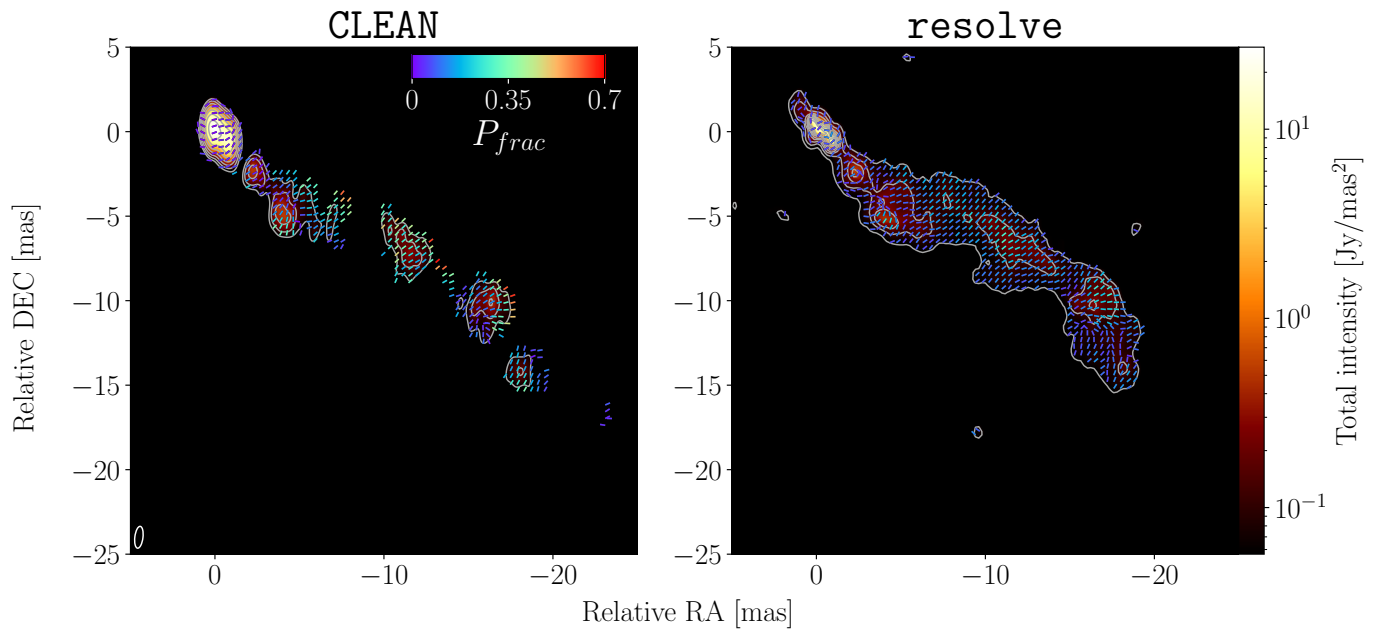


**Fig. 3.** Comparison between the 3C273 VLBA CLEAN and resolve posterior mean linear polarization reconstructions at 15 GHz. Colored ticks indicate EVPAs, with colors corresponding to the fractional linear polarization  $P_{\text{frac}}$ . The contours representing the total intensity of corresponding images increase by a factor of 2, starting from 1% of the peak CLEAN total intensity.

28 January 2017 (Lister et al. 2018) in order to demonstrate that **resolve** is able to infer D-terms per intermediate frequency (IF) from a source with complex structure. The data have 8 IFs (32MHz each) and the total bandwidth is 256MHz.

We reconstructed the **resolve** Stokes images with a spatial domain of  $256 \times 256$  and a field of view of  $50 \text{ mas} \times 50 \text{ mas}$ . For the **resolve** reconstruction, we added a 10 % systematic error budget in the data. The reduced  $\chi^2$  of the **resolve** reconstruction was 1.2, and the number of posterior samples was 20. The wall-clock time for the **resolve** reconstruction was around 5 hours on a single node of the MPIFR cluster with 10 MPI (Message Passing Interface) tasks.

We assumed that Stokes images do not vary over frequencies due to the narrow bandwidth (256 MHz), and performed antenna gain self-calibration and leakage calibration per IF. For the absolute EVPA calibration, we applied the same correction value from the MOJAVE team for the CLEAN reconstruction. The model parameters for polarization imaging prior, gain prior, and D-term prior for the 3C273 VLBA data can be found in Table A.1 and Table A.2.

Figure 3 shows a comparison of linear polarization reconstructions from CLEAN and the **resolve** posterior mean. EVPA colors correspond to the fractional linear polarization, and contours represent the total intensity of the corresponding images. The CLEAN images are taken from the MOJAVE archive<sup>2</sup>. For the CLEAN reconstruction, the MOJAVE team performed self-calibration and image reconstruction using the DIFMAP software (Shepherd 1997) and the LPCAL task (Leppanen et al. 1995) in the AIPS software (Greisen 2003) for polarization calibration. The D-term solutions using LPCAL are the median solution values from all sources in the epoch after removing obvious outliers (Lister & Homan 2005).

In the core region, the **resolve** image shows improved resolution compared to the core in the CLEAN image. The extended total intensity emission in the **resolve** image is overall consistent with the CLEAN reconstruction but it looks more continuous

since the spatial correlations between pixels are inferred from the data in **resolve**. We note that it is also possible to use an over-resolved CLEAN beam to obtain a CLEAN image with higher resolution. However, an image convolved with an over-resolved CLEAN beam cannot adequately describe the continuous extended jet and it may result in unrealistic fractional linear polarization ( $I < \sqrt{Q^2 + U^2 + V^2}$ ). In contrast to CLEAN, **resolve** can describe complex source structure spanning a range of spatial scales using the Gaussian process sky prior we described, which is aware of spatial correlations of the polarized flux while ensuring the polarization constraints at each image pixel individually.

The linear polarization comparison between CLEAN and **resolve** shows noticeable differences. The fractional linear polarization on the edges of linearly polarized emission in the CLEAN reconstruction is relatively higher than that in the **resolve** reconstruction. The discrepancy may result from the lack of a polarization constraint in the CLEAN imaging prior or biases from the similarity approximation in CLEAN-based polarization calibration. Encoding the polarization constraint that the maximum linear polarization is 100 % in the prior facilitates physically sensible reconstruction consistent with the theoretical fractional linear polarization for optically thin synchrotron radiation from non-thermal electrons with a power law distribution of energies (up to 75 %; Rybicki & Lightman (1979)).

The EVPA pattern is generally consistent except for the core region due to the improved resolution in the **resolve** image. Both images show the rotational EVPA structure at the core but the **resolve** image exhibits thinner emission structures that show more abrupt changes. Figure D.1 shows the 3C273 **resolve** EVPA standard deviation. We note that a robust rotation measure can be estimated using the Bayesian approach (Vogt & Enßlin 2005). A detailed investigation of Bayesian rotation measure analysis using our method is left for future work.

For the leakage calibration, a total of 160 D-terms (2 polarization modes  $\times$  10 antennas  $\times$  8 IFs) are inferred since the D-terms in MOJAVE observations with VLBA at 15 GHz tend to be

<sup>2</sup> <https://www.cv.nrao.edu/MOJAVE/>

different per IF. This approach of reconstructing D-terms per IF is highly desirable, especially for wide-band observations, as the signal path for each IF is different which can result in changes to the D-terms for each IF separately. We also note that base-band boundaries can cause jumps in leakage that will also differ for the individual IFs (Martí-Vidal et al. 2021).

In Figure C.1, the resolve D-term posterior means and D-terms obtained using the `LPCAL` software are shown to be consistent with each other, as they are strongly correlated. It is important to note that the resolve D-term solutions are from 3C273 data only and D-terms using `LPCAL` are the median values of D-term solutions from multiple sources. The results indicate that our Bayesian polarization calibration method is able to estimate reliable D-terms from data with complex source structures. A more detailed analysis with additional data sets is deferred to future work.

#### 4.2. OJ287 GMVA+ALMA observation at 86 GHz

Zhao et al. (2022) report the GMVA+ALMA observation of the blazar OJ 287 at 86 GHz on 2. April 2017. The blazar OJ 287 is a supermassive binary black hole candidate showing quasiperiodic optical outbursts with a period of about 12 years (Sillanpää et al. 1988). GMVA observations jointly with the phased ALMA provide high fidelity images due to the improved sensitivity and long north-south baselines (Issaoun et al. 2019; Zhao et al. 2022; Lu et al. 2023; Kim et al. 2025). However, polarization calibration and imaging for mm-VLBI observations are demanding due to the low S/N of the polarized signals, tropospheric phase corruption, and heterogeneous antenna statistics, such as in GMVA+ALMA data.

We revisit the GMVA+ALMA observation of the blazar OJ 287 at 86 GHz in Zhao et al. (2022) to validate our Bayesian polarization calibration and imaging method using pre-calibrated data. For polarization calibration, robust gain self-calibration is required due to the degeneracy between D-terms and gains. Kim et al. (2024, 2025) validate the `resolve` self-calibration methods with mm-VLBI data sets. Reconstructed antenna gain solutions from the VLBA M87 observation in 2013 at 43GHz indicate that gain solutions from a homogeneous array with high S/N are consistent among `CLEAN`, `ehtim`, and `resolve` methods (Kim et al. 2024). However, `CLEAN` self-calibration utilizes a crude regularizer (e.g., a uniform solution interval for different antenna gain solutions) and often flags a significant fraction of the data. Therefore, those limitations may hinder robust self-calibration for mm-VLBI observations.

To mitigate this issue, we employed different correlation kernels for antenna gain amplitude solutions in order to take into account heterogeneous array sensitivity. For the gain phase prior, we utilized uncorrelated normally distributed phases due to the short phase coherence time in GMVA observations at 86 GHz (Kim et al. 2025). Employing a different gain amplitude kernel per antenna is analogous to setting up different solution interval constraints per antenna in self-calibration. In `resolve`, the time correlations in the gain solutions are inferred from the data in an automated fashion and the large uncertainties of particular data points are taken into account naturally in the Bayesian framework. Therefore, we are able to perform more robust self-calibration without flagging a significant number of the data points compared to `CLEAN`-based self-calibration methods. Furthermore, the large gain uncertainties inherent to mm-VLBI observations are explicitly accounted for and propagated into the image domain. As a result, the reliability of calibration and imaging is quantified through uncertainty estimation.

Polarization calibration for mm-VLBI data sets presents several additional challenges. In mm-VLBI, we often use the target data for D-term calibration due to a lack of point-like calibrators. Polarization leakages tend to be higher in mm-VLBI than in cm-VLBI, and the high resolution often reveals complex source polarization structures. Thus, precise D-term calibration is crucial to obtain reliable polarimetric images, and accurate polarimetric images, in turn, improve D-term calibration. However, in conventional polarization calibration methods, utilizing the similarity approximation or `CLEAN` images as a prior hinders the reconstruction of complex polarization structures since a few sub-components in the similarity approximation and the collection of delta components in the `CLEAN` reconstruction cannot accurately represent the extended emission and complex source structures that are smaller than the `CLEAN` beam. On the other hand, in `resolve`, polarization imaging models with complex source structures, satisfying the polarization constraint and consistent with the data, are utilized for more robust polarization calibration.

The data are time-averaged with 15 seconds and frequency-averaged for `ehtim` and `resolve` software, since the antenna leakages in the data are similar over frequencies (Zhao et al. 2022). For the `CLEAN` image, self-calibration and image reconstruction were performed using the `DIFMAP` software and the `LPCAL` method of the `AIPS` software was used for leakage calibration using 4 individual intermediate frequencies (IFs). For the `ehtim` reconstruction, self-calibration and polarization calibration were performed in an iterative fashion using the `ehtim` software. The details regarding the `CLEAN` and `ehtim` polarization calibration and image reconstructions can be found in Zhao et al. (2022).

For the `resolve` reconstruction, Stokes I, Q, U, and V images with a spatial domain of  $256 \times 256$  pixels and a field of view of  $500 \mu\text{as} \times 500 \mu\text{as}$ , as well as gain solutions with a time interval of 15 seconds and leakage solutions, are inferred simultaneously. The reduced  $\chi^2$  of the `resolve` reconstruction was 1.2, and the number of posterior samples was 100. The wall-clock time for the `resolve` reconstruction was around 8.5 hours on a single node of the MPIfR cluster with 25 MPI tasks. The model parameters for polarization imaging prior, gain prior, and D-term prior for the OJ287 GMVA+ALMA data can be found in Table A.3 and Table A.4.

Figure 4 depicts the total intensity with EVPAs of the blazar OJ287 at 86 GHz using three different imaging algorithms: `CLEAN`, `ehtim` from Zhao et al. (2022), and `resolve`. All three image reconstructions show three main components in the total intensity and diverging EVPAs in the north-west component. Furthermore, the curved jet (middle component) from the core (south-east component) is recognizable only in the `ehtim` and `resolve` images. In contrast, `CLEAN` has limitations in reconstructing smaller scale structures than the `CLEAN` beam. The `ehtim` and `resolve` images show better resolution than the `CLEAN` image because forward modeling permits partial removal of the observational point spread function during the data inversion process. The `ehtim` image exhibits higher resolution than the `resolve` image, since the sparsity promoting regularizers in `ehtim` tend to produce extremely sharp structures.

For polarization imaging, polarization constraints are encoded in `resolve` and `ehtim`. We performed the absolute EVPA calibration using the reported integrated EVPA of ALMA-only OJ287 image at 86 GHz in Goddi et al. (2021). The details of the absolute EVPA calibration method can be found in Appendix B. In Figure 4, the EVPAs in the north-west jet component diverge in all three images. The fractional linear polarization along

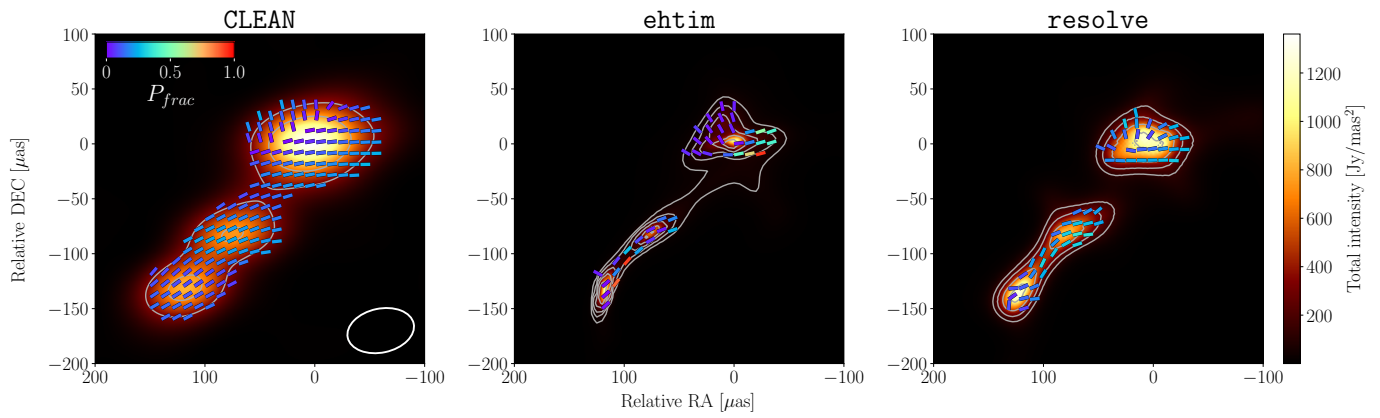


**Fig. 4.** Comparison among the OJ287 GMVA+ALMA CLEAN, ehtim, and resolve posterior mean linear polarization reconstructions at 86 GHz. Colored ticks indicate EVPAs, with colors corresponding to the fractional linear polarization  $P_{\text{frac}}$ . The contours representing the total intensity of the corresponding images increase by a factor of 2, starting from 10% of the peak resolve posterior mean total intensity. All images were processed by Gaussian interpolation.

the north-east direction in the diverging jet component increases gradually in the images from CLEAN and resolve, whereas the ehtim image shows a nearly monotonous fractional linear polarization. In the ehtim image, there are extremely highly polarized pixels ( $P_{\text{frac}} > 99\%$ ) that may be imaging artifacts caused by the sparsity regularizers. A high fractional linear polarization ( $> 75\%$ ) indicates optically thin synchrotron radiation from a uniform magnetic field and the absence of Faraday depolarization. However, such a scenario is unrealistic, since the EVPA reconstruction of OJ287 shows complex structure indicating a non-uniform magnetic field. We note that the Faraday rotation of OJ287 from the ALMA-only observation is  $3.05 \pm 0.62 \times 10^3 \text{ rad m}^{-2}$  (Goddi et al. 2021), which is relatively small, Faraday depolarization therefore can be negligible.

The south-east core component and the middle jet component show EVPAs along the jet direction. This indicates toroidal magnetic fields, given that the relatively small rotation measure from the ALMA observation (Goddi et al. 2021). In the ehtim and resolve images, we see bending EVPA patterns, and the pattern is more wiggling in the resolve image. The diverging EVPA pattern in the north-west jet component can be explained by oblique or recollimation shocks (Zhao et al. 2022). Figure D.2 shows the OJ287 resolve EVPA posterior standard deviation.

Figure 5 shows the amplitude gain posterior distribution. Different correlation kernels per antenna are employed to infer different temporal correlation structure arising from the heterogeneous antenna sensitivities. We utilized a uncorrelated phase gain prior since the phase coherence time is comparable to the averaging time (15 seconds).

Figure 6 depicts a comparison between the resolve D-term posterior distributions and reconstructed D-terms using ehtim. The resolve and ehtim D-terms are broadly consistent. In Figure C.2, cross correlation plots between resolve posterior D-terms and ehtim reconstructed D-terms are shown. They exhibit strong positive correlations, but some antennas (e.g., PT) show weaker positive correlations. This discrepancy between resolve and ehtim results from the highly corrupted phases at 3mm and the different self-calibration and flagging routines used. For polarization calibration and imaging, ehtim used 8 antennas out of 13, whereas resolve utilized all antennas (YS observed only single polarization; therefore, we show the resolve D-terms for 12 antennas). In resolve, non-Gaussian leakage posterior distributions were obtained using the geoVI method. A few antennas (e.g., BR and ON) exhibit higher uncertainty in

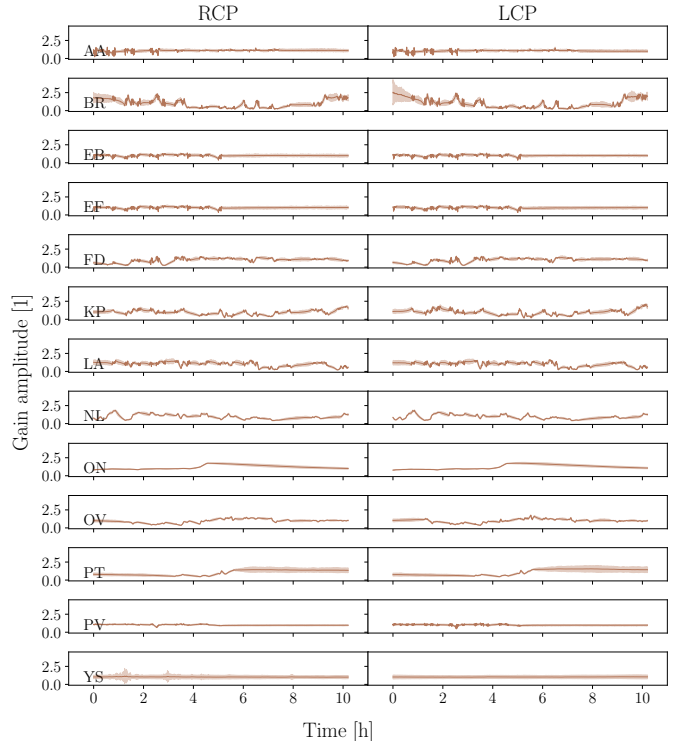


**Fig. 5.** Posterior amplitude gains of the OJ287 GMVA+ALMA observation using resolve. The solid line represents the amplitude gain posterior mean with a semi-transparent standard deviation. Each row represents an individual antenna with corresponding abbreviated name in the bottom left corner of each RCP plot.

the D-term phase due to highly corrupted visibility phases. The ehtim D-terms are overall consistent with D-terms obtained from the LPCAL software (Zhao et al. 2022). In conclusion, the D-term solutions are in good agreement across the resolve, ehtim, and LPCAL methods.

We note that RML methods can be interpreted as maximum a-posteriori (MAP) estimation in Bayesian language (Kim et al. 2024). However, the point estimation cannot represent calibration solutions with high uncertainties well, and the MAP estimation is prone to overfitting the data. Furthermore, ehtim does not support multi-scale bases functions. In contrast to resolve,

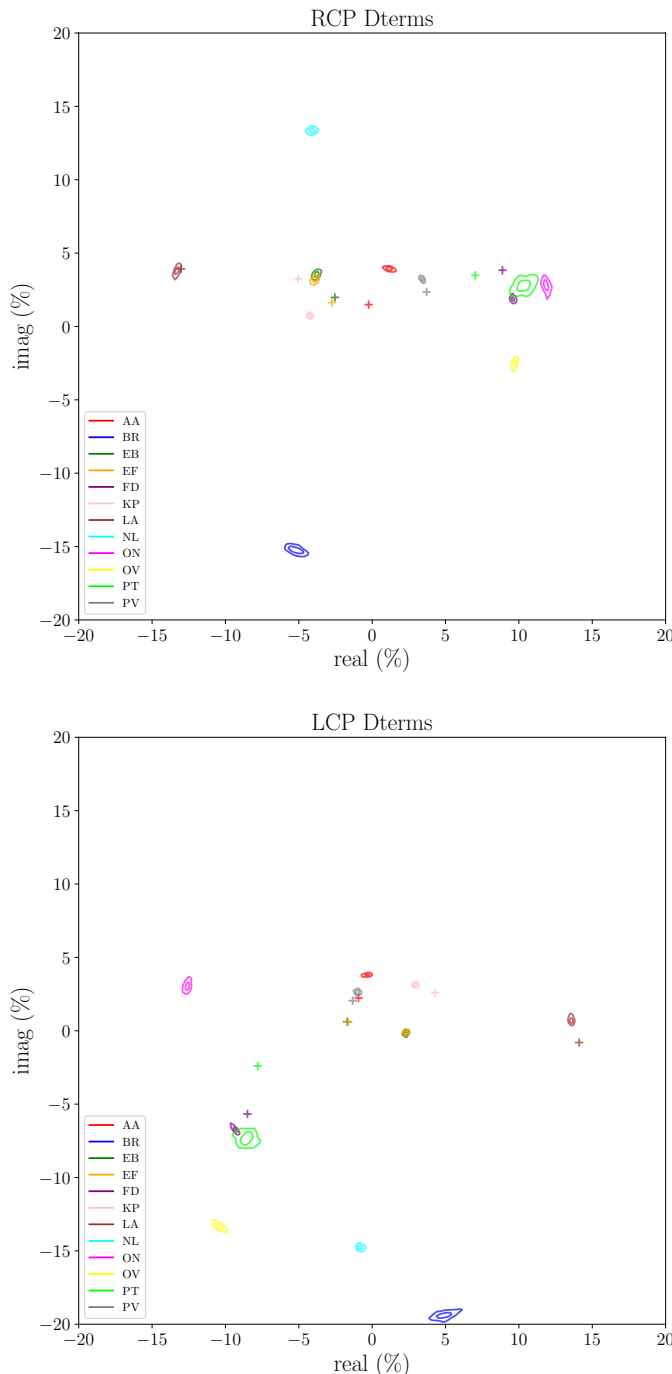


**Fig. 6.** Comparison between OJ287 GMVA+ALMA D-term posterior distributions using `resolve` and D-term solutions using `ehtim`. Contours show  $1\sigma$  and  $2\sigma$  cumulative regions of `resolve` posterior D-terms using Gaussian kernel density estimation. The plus signs correspond to the reconstructed D-terms using `ehtim`.

it tends to produce extremely sharp features. Different correlation structures between the core and jet cannot be adequately described due to the sparsity promoting priors, such as the  $l_1$ -norm, total variation (TV), and total squared variation (TSV). Employing extremely sharp images as a model in polarization calibration may result in biased D-terms and polarization images. A more detailed discussion of the Bayesian interpretation of regularizers in RML method can be found in the Appendix B of Kim et al. (2024).

In short, the `resolve` reconstructions of 3C273 at 15 GHz OJ 287 at 86 GHz demonstrate that our Bayesian polarization calibration and imaging pipeline can obtain reliable super-resolution polarimetric images, D-terms and gain solutions from VLBI data. Reconstructed Stokes images are utilized as a polarization calibration model, enabling to obtain more complex polarization structures than conventional CLEAN-based methods. Uncertainty estimation of reconstructed images and calibration solutions in `resolve` is especially beneficial in mm-VLBI due to the high calibration uncertainties from tropospheric phase corruptions and antenna leakages. In our method, calibration uncertainties are accounted for in our reconstructed images and we are able to quantify the reliability of Stokes images and calibration solutions.

## 5. Conclusions

In this work, we have presented a novel Bayesian polarization calibration and imaging method using the `resolve` algorithm. Our method can simultaneously reconstruct high-resolution polarimetric images satisfying the polarization constraint ( $I \geq \sqrt{Q^2 + U^2 + V^2}$ ), antenna-based gains, and polarization leakages from the entire data set. The polarization calibration is based on the reconstructed Stokes images instead of the similarity approximation used in traditional approaches, which does not hold for complex polarized emission patterns. Therefore, we can reconstruct reliable polarimetric images with complex structures and more robust calibration solutions, consistent with the entire data set. Moreover, multi-source and multi-IF polarization calibration is supported owing to the scalability of `resolve`, achieved through variational inference methods (Knollmüller & Enßlin 2019; Frank et al. 2021).

We have demonstrated our method with synthetic and real observations. Examples using the quasar 3C273 MOJAVE VLBA data at 15 GHz and the blazar OJ287 GMVA+ALMA observation at 86 GHz show that `resolve` can reconstruct polarimetric images with super-resolution (Honma et al. 2014), revealing structures below the synthesized beam, which is the resolution limit of the conventional CLEAN-based methods. The fractional linear polarization in `resolve` images is consistent with the theoretical estimation for synchrotron radiation (< 75%) in AGN jets.

Reconstructed D-terms obtained with `resolve` are consistent with those from the conventional CLEAN-based method and the RML-based method `ehtim`. Furthermore, our RIME-based Bayesian polarization calibration and imaging method is able to reconstruct D-term solutions from target data with complex source structure without using calibrators.

Validation with synthetic and real data sets indicates that incorporating polarization calibration into imaging is beneficial for sparse and noisy VLBI data sets in order to estimate reliable and reproducible calibration solutions and images. Calibration uncertainties are explicitly taken into account in our final `resolve` results, and the reliability of the gain and leakage solutions was estimated. For future work, the EVPA posterior distribution can be utilized for rotation measure analysis, and frequency-dependent D-term calibration within the Bayesian framework should be investigated for wide-band radio interferometric observations. The pipeline is publicly accessible at [https://github.com/JongseoKim/resolve\\_polcal](https://github.com/JongseoKim/resolve_polcal)

*Acknowledgements.* We thank Yuri Kovalev for comments on the manuscript and providing the MOJAVE data, Guang-Yao Zhao and Jose Gomez for providing the GMVA+ALMA OJ287 data. J. K. received financial support for this

research from the International Max Planck Research School (IMPRS) for Astronomy and Astrophysics at the Universities of Bonn and Cologne. This work was supported by the M2FINDERS project funded by the European Research Council (ERC) under the European Union's Horizon 2020 Research and Innovation Programme (Grant Agreement No. 101018682). J. R. acknowledges financial support from the German Federal Ministry of Education and Research (BMBF) under grant 05A23WO1 (Verbundprojekt D-MeerkAT III)

## References

Arras, P., Baltac, M., Enßlin, T., et al. 2019a, NIFTy5: Numerical Information Field Theory v5

Arras, P., Bester, H. L., Perley, R. A., et al. 2021, *Astronomy & Astrophysics*, 646, A84

Arras, P., Frank, P., Leike, R., Westermann, R., & Enßlin, T. A. 2019b, *A&A*, 627, A134

Arras, P., Roth, J., Reinecke, M., et al. 2025, arXiv e-prints, arXiv:2504.00227

Asada, K., Inoue, M., Kameno, S., & Nagai, H. 2008, *ApJ*, 675, 79

Birdi, J., Repetti, A., & Wiaux, Y. 2018, *MNRAS*, 478, 4442

Birdi, J., Repetti, A., & Wiaux, Y. 2020, *MNRAS*, 492, 3509

CASA Team, Bean, B., Bhatnagar, S., et al. 2022, *PASP*, 134, 114501

Cornwell, T. J. 2008, *IEEE Journal of Selected Topics in Signal Processing*, 2, 793

Cotton, W. D. 1993, *AJ*, 106, 1241

Event Horizon Telescope Collaboration. 2025, arXiv e-prints, arXiv:2509.24593

Event Horizon Telescope Collaboration, Akiyama, K., Alberdi, A., et al. 2024, *ApJ*, 964, L25

Event Horizon Telescope Collaboration, Akiyama, K., Alberdi, A., et al. 2019, *ApJ*, 875, L1

Event Horizon Telescope Collaboration, Akiyama, K., Algaba, J. C., et al. 2021, *ApJ*, 910, L12

Frank, P., Leike, R., & Enßlin, T. A. 2021, *Entropy*, 23, 853

Gabuzda, D. C., Roche, N., Kirwan, A., et al. 2017, *MNRAS*, 472, 1792

Goddi, C., Martí-Vidal, I., Messias, H., et al. 2021, *ApJ*, 910, L14

Greisen, E. W. 2003, in *Astrophysics and Space Science Library*, Vol. 285, Information Handling in Astronomy - Historical Vistas, ed. A. Heck, 109

Hamaker, J. P., Bregman, J. D., & Sault, R. J. 1996, *A&AS*, 117, 137

Hamaker, J. P., Bregman, J. D., & Sault, R. J. 1996, *Astronomy and Astrophysics Supplement Series*, 117, 137

Honma, M., Akiyama, K., Uemura, M., & Ikeda, S. 2014, *PASJ*, 66, 95

Hovatta, T., Lister, M. L., Aller, M. F., et al. 2012, *AJ*, 144, 105

Issaoun, S., Johnson, M. D., Blackburn, L., et al. 2019, *ApJ*, 871, 30

Janssen, M., Goddi, C., van Bemmel, I. M., et al. 2019, *A&A*, 626, A75

Jones, R. C. 1941, *Journal of the Optical Society of America (1917-1983)*, 31, 488

Kim, J.-S., Müller, H., Nikonorov, A. S., et al. 2025, *A&A*, 696, A169

Kim, J.-S., Nikonorov, A. S., Roth, J., et al. 2024, *A&A*, 690, A129

Knollmüller, J. & Enßlin, T. A. 2019, arXiv e-prints, arXiv:1901.11033

Knollmüller, J. & Enßlin, T. A. 2018, Encoding prior knowledge in the structure of the likelihood

Leppanen, K. J., Zensus, J. A., & Diamond, P. J. 1995, *AJ*, 110, 2479

Lister, M. L., Aller, M. F., Aller, H. D., et al. 2018, *ApJS*, 234, 12

Lister, M. L. & Homan, D. C. 2005, *AJ*, 130, 1389

Lu, R.-S., Asada, K., Krichbaum, T. P., et al. 2023, *Nature*, 616, 686

Martí-Vidal, I. & Marcaide, J. M. 2008, *A&A*, 480, 289

Martí-Vidal, I., Mus, A., Janssen, M., de Vicente, P., & González, J. 2021, *A&A*, 646, A52

McMullin, J. P., Waters, B., Schiebel, D., Young, W., & Golap, K. 2007, in *Astronomical Society of the Pacific Conference Series*, Vol. 376, *Astronomical Data Analysis Software and Systems XVI*, ed. R. A. Shaw, F. Hill, & D. J. Bell, 127

Park, J., Asada, K., & Byun, D.-Y. 2023, *ApJ*, 958, 27

Park, J., Asada, K., Nakamura, M., et al. 2021a, *ApJ*, 922, 180

Park, J., Byun, D.-Y., Asada, K., & Yun, Y. 2021b, *ApJ*, 906, 85

Pesce, D. W. 2021, *AJ*, 161, 178

Popkov, A. V., Kovalev, Y. Y., Petrov, L. Y., & Kovalev, Y. A. 2021, *AJ*, 161, 88

Pushkarev, A. B., Aller, H. D., Aller, M. F., et al. 2023, *MNRAS*, 520, 6053

Raymond, A. W., Doeleman, S. S., Asada, K., et al. 2024, *AJ*, 168, 130

Roth, J., Arras, P., Reinecke, M., et al. 2023, *A&A*, 678, A177

Roth, J., Frank, P., Bester, H. L., et al. 2024, *A&A*, 690, A387

Rybicki, G. B. & Lightman, A. P. 1979, *Radiative processes in astrophysics*

Sélig, M., Bell, M. R., Junklewitz, H., et al. 2013, *A&A*, 554, A26

Shepherd, M. C. 1997, in *Astronomical Society of the Pacific Conference Series*, Vol. 125, *Astronomical Data Analysis Software and Systems VI*, ed. G. Hunt & H. Payne, 77

Sillanpää, A., Haarala, S., Valtonen, M. J., Sundelius, B., & Byrd, G. G. 1988, *ApJ*, 325, 628

Smirnov, O. M. 2011, *A&A*, 527, A106

Smirnov, O. M. 2011, *Astronomy & Astrophysics*, 527, A106

Thompson, A. R., Moran, J. M., & Swenson, Jr., G. W. 2017, *Interferometry and Synthesis in Radio Astronomy*, 3rd Edition

Virtanen, P., Gommers, R., Oliphant, T. E., et al. 2020, *Nature Methods*, 17, 261

Vogt, C. & Enßlin, T. A. 2005, *A&A*, 434, 67

Zhao, G.-Y., Gómez, J. L., Fuentes, A., et al. 2022, *ApJ*, 932, 72

## Appendix A: Hyperparameter setup

## Appendix B: Absolute EVPA calibration

Most VLBI observations use circular polarization feeds. Therefore, we need to constrain the arbitrary phase difference between the right and left circular polarization feeds (RCP and LCP) at each frequency in the fully station based approach to polarization classification and calibration (Cotton 1993; Leppanen et al. 1995). This process is called absolute EVPA calibration. The simplest approach to determining this phase offset is to use a trusted external observation as an ‘anchor’. External anchors are typically observations with a single dish, an interferometer with linear polarization feeds, or an observation that has already calibrated the phase difference between RCP and LCP independently. This method relies on the assumption that the signal of a ‘target’ observation is similar to that of the anchoring observation, in both time and the physical structure of the emission. As such, the best calibrated sources for absolute EVPA calibration have the following three characteristics;

1. The source has sufficient linear polarization in both the target observation and anchor observation.
2. The source is not highly variable in time; as such does not vary between the two observations.
3. The source is compact; this is particularly relevant when comparing a target VLBI observation against single dish or unresolved non-VLBI observations as we assume the emission from both observations comes from the same physical structure of the source.

To compute the RCP-LCP phase correction we take twice the EVPA offset between the target and anchor observations. Typically, the EVPA offset is found by calculating the integrated Stokes Q and U flux density of both observations and calculating an integrated EVPA as  $EVPA = 0.5 \arctan[U/Q]$ . This can be done by only considering Stokes Q and U emission that is co-spatial with Stokes I emission to ensure a direct comparison between the target and anchor.

For our reconstruction of OJ287 in Figure 4, we calculated the integrated EVPA of our reconstructed resolve image of Stokes Q and U and compared it to ALMA observations with the EVPA - 69.69° at 86.3 GHz in Goddi et al. (2021). From this we found an EVPA correction of -16.07° based on the OJ287 resolve integrated EVPA and ALMA-only EVPA.

## Appendix C: D-term cross correlation plots

## Appendix D: EVPA posterior standard deviation plots

**Table A.1.** Model parameters for the resolve 3C273 polarization imaging priors  $s$ ,  $q$ ,  $u$ , and  $v$ .

	$s$ mean	$s$ std	$q, u$ mean	$q, u$ std	$v$ mean	$v$ std
Offset	35.0	—	0.0	—	0.0	—
Zero mode variance	1.0	0.1	0.01	0.01	0.001	0.001
Fluctuations	3.0	1.0	0.05	0.05	0.005	0.005
Flexibility	1.2	0.4	0.1	0.1	0.1	0.1
Asperity	—	—	—	—	—	—
Average slope	-3.0	1.0	-3.0	1.0	-3.0	1.0

**Table A.2.** Model parameters for the resolve 3C273 log-amplitude gain prior  $\lambda$ , phase gain prior  $\phi$ , log-amplitude D-term prior  $a$ , and phase D-term prior  $b$ .

	$\lambda$ mean	$\lambda$ std	$\phi$ mean	$\phi$ std	$a$	$b$
Offset	0.0	—	0.0	—	Mean	-2.5
Zero mode variance	0.1	0.01	0.2	0.1	Std	1.0
Fluctuations	0.2	0.1	0.2	0.1		
Flexibility	0.5	0.2	0.5	0.2		
Asperity	None	None	None	None		
Average slope	-3.0	1.0	-3.0	1.0		

**Table A.3.** Model parameters for the resolve OJ287 polarization imaging priors  $s$ ,  $q$ ,  $u$ , and  $v$ .

	$s$ mean	$s$ std	$q, u$ mean	$q, u$ std	$v$ mean	$v$ std
Offset	38.0	—	0.0	—	0.0	—
Zero mode variance	1.0	0.1	0.01	0.01	0.001	0.001
Fluctuations	3.0	1.0	0.05	0.05	0.005	0.005
Flexibility	1.2	0.4	0.1	0.1	0.1	0.1
Asperity	—	—	—	—	—	—
Average slope	-3.0	0.5	-3.0	0.5	-3.0	0.5

**Table A.4.** Model parameters for the resolve OJ287 log-amplitude gain prior  $\lambda$ , phase gain prior  $\phi$ , log-amplitude D-term prior  $a$ , and phase D-term prior  $b$ .

	$\lambda$ mean	$\lambda$ std	$\phi$	$a$	$b$
Offset	0.0	—	Mean	0.0	-2.5
Zero mode variance	1e-3	1e-6	Std	2.0	0.5
Fluctuations	0.2	0.1			
Flexibility	0.5	0.2			
Asperity	None	None			
Average slope	-3.0	1.0			

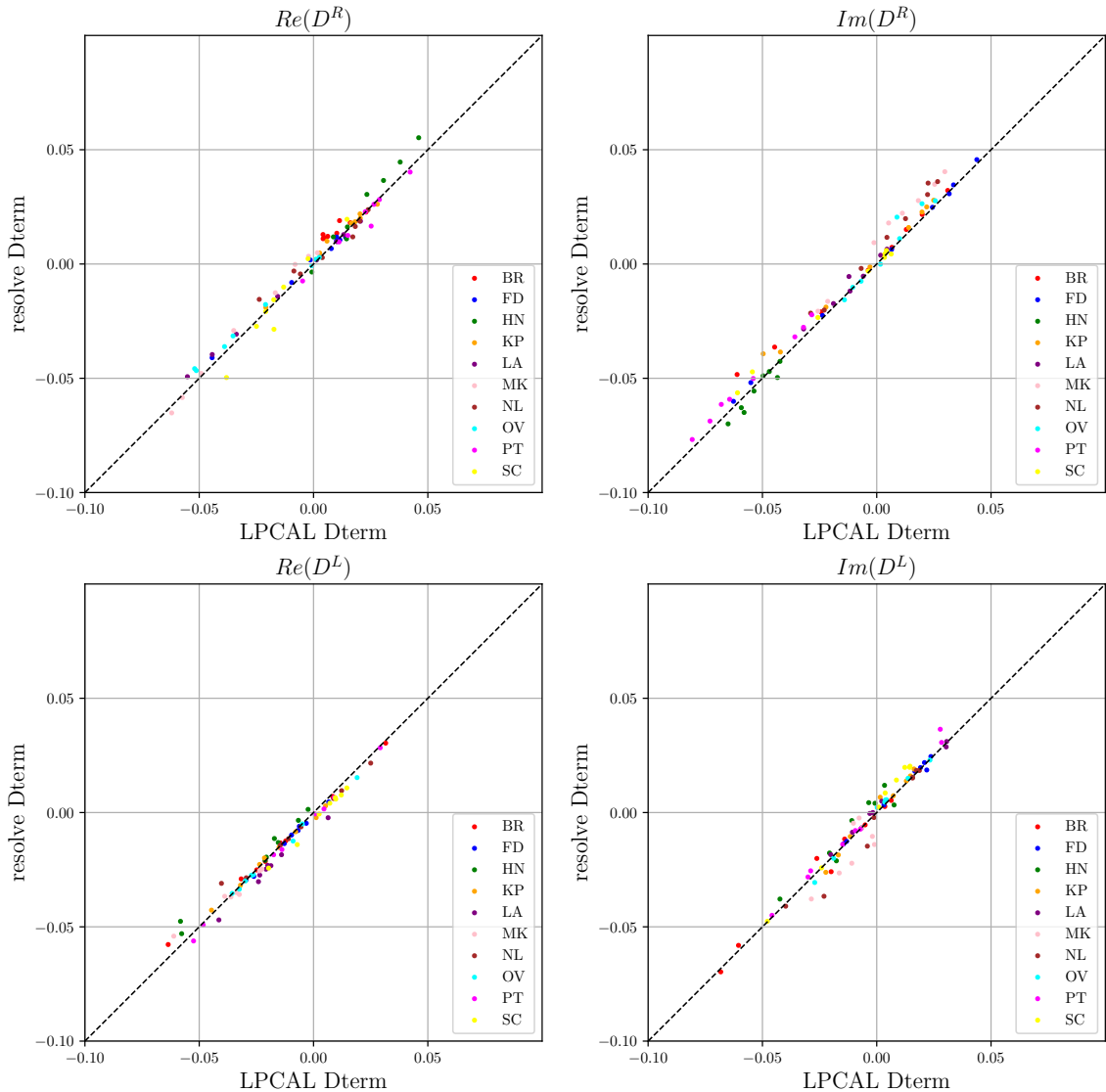


**Fig. C.1.** Cross correlation plots between 3C273 resolve posterior mean D-terms and LPCAL D-terms.

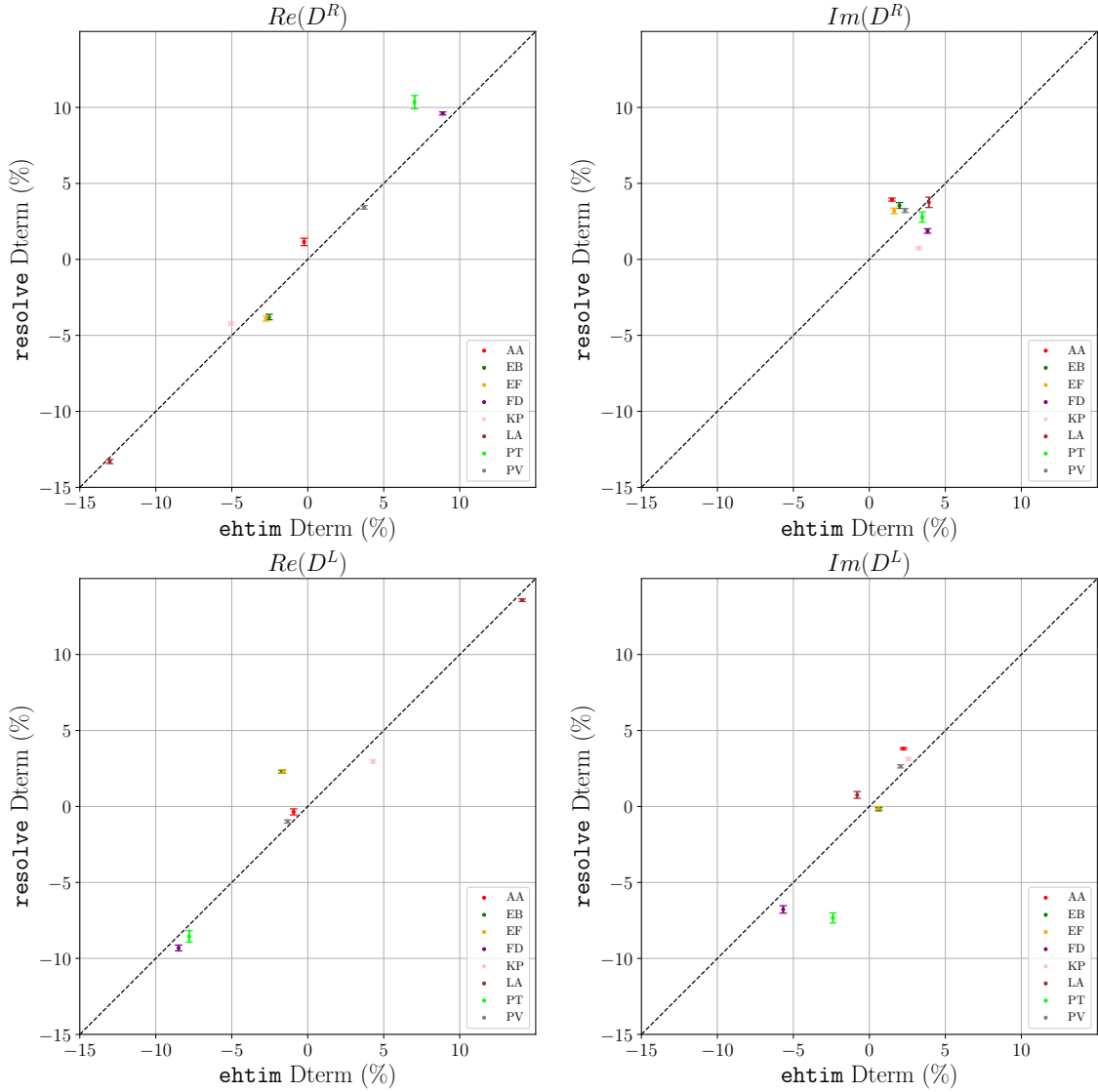


**Fig. C.2.** Cross correlation plots between OJ287 GMVA+ALMA D-term posterior means using `resolve` and D-term solutions using `ehtim`.

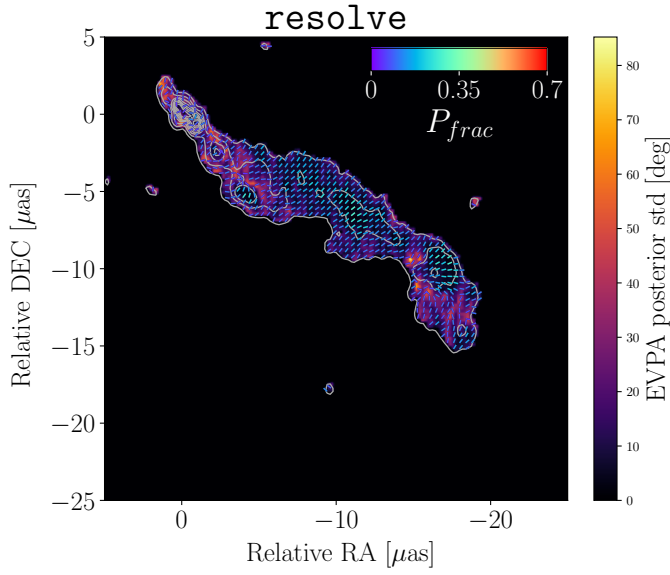


**Fig. D.1.** EVPA posterior standard deviation map of the 3C273 observation at 15GHz using `resolve`. The contours representing the total intensity `resolve` posterior mean image increase by a factor of 2, starting from 1% of the peak CLEAN total intensity.

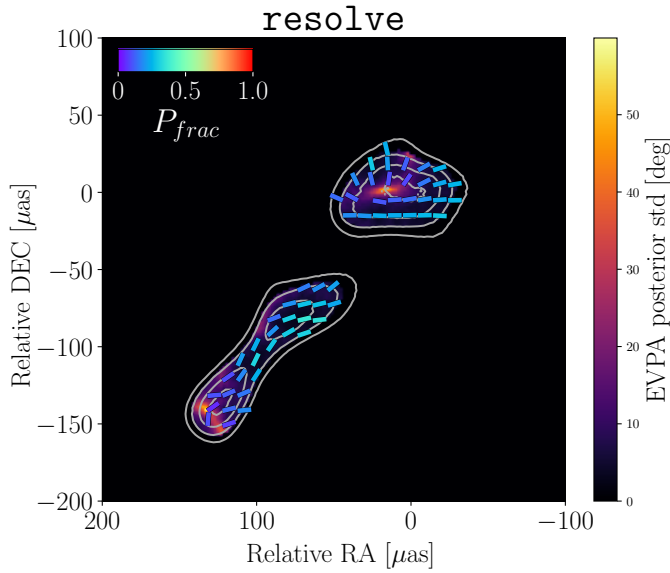


**Fig. D.2.** EVPA posterior standard deviation map of the OJ287 GMVA+ALMA observation at 86GHz using `resolve`. The contours representing the total intensity `resolve` posterior mean image increase by a factor of 2, starting from 10% of the peak `resolve` posterior mean total intensity.